A Comparative Study of Compressive Effects on the Morphology and Performance of Carbon Paper and Cloth Electrodes in Redox Flow Batteries

Citation: Tenny, Kevin M, Greco, Katharine V, van der Heijden, Maxime, Pini, Tommaso, Mularczyk, Adrian et al. 2022. "A Comparative Study of Compressive Effects on the Morphology and Performance of Carbon Paper and Cloth Electrodes in Redox Flow Batteries." Energy Technology, 10 (8).

As Published: 10.1002/ENTE.202101162

Publisher: Wiley

Persistent URL: https://hdl.handle.net/1721.1/145736

Version: Final published version: final published article, as it appeared in a journal, conference proceedings, or other formally published context

Nanocharacterization by TEM and AFM

We offer a wide range of TEM and AFM tools, from TEM grids and finders to AFM substrates and grippers.

Available in a wide variety of designs and materials to support your work, select from a broad range of mesh sizes, specimen supporting films, and materials that perfectly suit the conditions of your TEM analysis.

TEM grid specifications:

Material	Mesh Size and Shape	Film Specifications
• Cu • Ni • Au • Mo • Cu/Pd	• Square or hexagonal • Single-hole grid (75 mm or 100 mm) • 100 • 150 • 200 • 300 • 400	• None • Continuous formvar film (thicknesses: 5-6 nm, 10 nm) • Lacey carbon film (average hole sizes: 50 nm, 100 nm, 150 nm, 100 mm, 150 mm) • Continuous amorphous carbon film (thicknesses: 10 nm, 20-30 nm) • Continuous formvar/ carbon film (thickness: 10nm formvar and 1nm carbon)

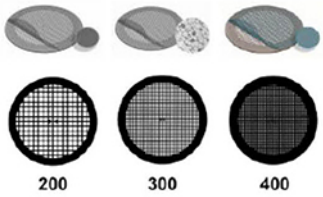

TEM finder grid specifications:

Material	Mesh Size	Film Specifications
• Cu • Ni • Au	• 135 • 200 • 300 • 400	• None • Continuous amorphous carbon film (thicknesses: 3-4 nm, 10 nm, 20-30 nm)

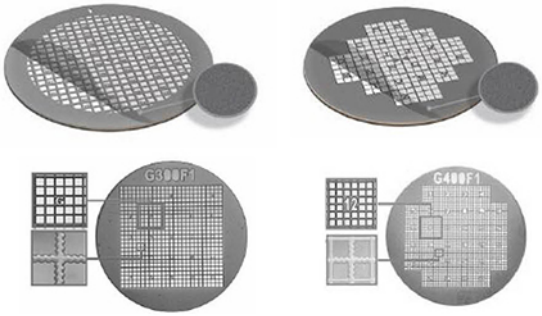

Supporting Tools for Nanomaterial Characterization

Our comprehensive range of supporting materials for nanomaterial characterization includes tweezers (sharp tip, disc gripper for AFM), TEM window grids (various thicknesses, 1 or 9 windows), a magnetic pick-up tool, a grid storage box, cryo-capsules, lift-out grids (Cu or Mo), AFM substrates (various dimensions), and much more.

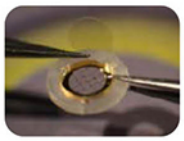

Explore our complete range of TEM grids on:
SigmaAldrich.com/nanocharacterization

MS_AD9792EN 43729 08/2022

MilliporeSigma is the U.S. and Canada Life Science business of Merck KGaA, Darmstadt, Germany.

Sigma-Aldrich®
Lab & Production Materials

Energy Technology
Generation, Conversion, Storage, Distribution
www.entechnol.de

A Comparative Study of Compressive Effects on the Morphology and Performance of Carbon Paper and Cloth Electrodes in Redox Flow Batteries

*Kevin M. Tenny, Katharine V. Greco, Maxime van der Heijden, Tommaso Pini, Adrian Mularczyk, Alexandru-Petru Vasile, Jens Eller, Antoni Forner-Cuenca, Yet-Ming Chiang, and Fikile R. Brushett**

Compressing porous carbon electrodes is a common approach to improve flow battery performance, but the resulting impact on electrode structure, fluid dynamics, and cell performance is not well understood. Herein, microtomographic imaging, load cell testing, and flow cell diagnostics are employed to characterize how compression-induced changes impact pressure drop, polarization, and mass-transfer scaling. Five different compressions are tested, spanning ranges typically used in literature, for AvCarb 1071 cloth (0%, 9%, 20%, 25%, 32%) and Freudenberg H23 paper (0%, 8%, 12%, 17%, 22%). It is found that the two electrode structures have distinct responses to compression, resulting in differing optimal conditions identified for each material; specifically, the Freudenberg H23 exhibits lower combined ohmic, charge-transfer, and mass-transport values at 8% compression, resulting in improved electrochemical performance across all compressive values, as compared to the optimal AvCarb 1071 compression (20%). Overall, Freudenberg H23 exhibits a greater sensitivity to compression with peak electrochemical activity correlating with increased permeability, whereas AvCarb 1071 is insensitive to compressive loads but produces lower electrochemical performance. Herein, the trade-offs of mechanical robustness on fluid-dynamic and electrochemical performance between the two electrodes are demonstrated by the aforementioned findings, suggesting each could be used for specific operating environments.

1. Introduction

Stationary energy storage solutions are expected to play a pivotal role in a sustainable and reliable energy economy with high fractions of low-carbon variable energy resources.[1] Redox flow batteries (RFBs) are an attractive technology platform, as the modular, flexible, and scalable system architecture offers a pathway to low-cost, long-duration energy storage;[2–6] however, current embodiments are considered too expensive for widespread adoption.[7] Advances in the design and engineering of the electrochemical flow cells that constitute the battery stack may enable significant cost reductions across multiple redox chemistries. Porous electrodes are a particularly promising area of investigation as they are responsible for several critical functions in the battery, including dispersing electrolyte, providing surface area and/or catalytic sites for reactions, and conducting electrons and heat.[8] Simple structural deformations to these electrodes can have marked effects on cell performance. Compression, as one specific approach,

K. M. Tenny, K. V. Greco, Y.-M. Chiang, F. R. Brushett
Joint Center for Energy Storage Research
Massachusetts Institute of Technology
Cambridge, MA 02139, USA
E-mail: brushett@mit.edu

K. M. Tenny, K. V. Greco, F. R. Brushett
Department of Chemical Engineering
Massachusetts Institute of Technology
Cambridge, MA 02139, USA

The ORCID identification number(s) for the author(s) of this article can be found under https://doi.org/10.1002/ente.202101162.

DOI: 10.1002/ente.202101162

M. van der Heijden, A. Mularczyk, A. Forner-Cuenca
Membrane Materials and Processes
Department of Chemical Engineering and Chemistry
Eindhoven University of Technology
5600 MB Eindhoven, The Netherlands

T. Pini
Department of Mechanical Engineering
Eindhoven University of Technology
5600 MB Eindhoven, The Netherlands

A. Mularczyk, A.-P. Vasile, J. Eller
Electrochemistry Laboratory
Paul Scherrer Institut
5232 Villigen-PSI, Switzerland

Y.-M. Chiang
Department of Materials Science & Engineering
Massachusetts Institute of Technology
Cambridge, MA 02139, USA

results in variations in electrode microstructure[9] and subsequently electrolyte mass transport,[10] affecting system properties such as electronic contact resistance, fluid-dynamic and electrochemical behavior, as well as potentially preventing cell/stack leaking. Previous studies have illustrated trade-offs between contact resistance and electrolyte mass transfer;[11–14] but as these publications have focused on optimization of a particular reactor configuration and chemistry, there is an opportunity to provide more generalized studies of the effect of compression on electrode properties and performance, especially for emerging materials, such as cloths.

While graphite felts have historically been the preferred electrode material in RFBs, engineering advances in both the peer-reviewed literature[15,16] and industry[17] have shown that the combination of thin carbon electrodes and structured flow fields, inspired by polymer–electrolyte fuel cells, can dramatically increase cell power output. Additionally, thinner electrodes (e.g., papers, cloths) may be more desirable for use in grid-scale flow battery systems due to smaller stack size, enabled by higher power output, and reduced parasitic losses due to pumping, provided by decreased pressure drop.[17] The compressive effects of cloths and papers have been studied in fuel cells;[18] though, to our knowledge, no one has compared incremental compressive effects on thin carbon-fiber-based materials when used as electrodes for redox active chemistries. Reported carbon cloth and paper compressions range from 10%–30%,[15,17,18] but it is unclear what performance changes should be expected across this range. Moreover, the compression–performance relationship is expected to be dependent on electrode and flow-field combination. In this work, we study the impact of compression on binder-free "model" carbon materials of distinct microstructures: a paper (Freudenberg H23) and a cloth (AvCarb 1071), using a combination of mechanical, microscopic, fluid-dynamic, and electrochemical methods. Specifically, we explore the fluid-dynamic relationships by extracting bulk scalar permeability values, and we approximate the electrochemically active surface area (ECSA) by measuring electrochemical double-layer capacitance (EDLC) both as a function of electrode compression values. To isolate mass-transfer effects, we use a kinetically facile redox couple dissolved in a low-viscosity nonaqueous electrolyte to evaluate the polarization performance in a single-electrolyte flow cell with a zero-gap architecture and an engineered flow field.[19] We subsequently fit the experimental data to a previously developed 1D macrohomogenous model[20] to extract mass-transfer relationships and demonstrate compression-specific improvements for each electrode. The overarching goal of this work is to describe the relationship between compression and cell performance in thin carbon materials and elucidate the changes in electrode structure from the physical deformations that may be used to identify impacts in electrochemical and fluid-dynamic performance.

2. Experimental Section

2.1. Materials and Set-up

Freudenberg H23 and AvCarb 1071 (used as received, Fuel Cell Store, College Station, Texas, USA) were used as the electrodes, and Daramic 175 (used as received, 175 μm nominal thickness, Daramic, LLC, Charlotte, NC) was used as the separator. Electrode thickness was measured with a Mitutoyo 0–1" flat anvil dial thickness gauge (±0.002" accuracy), and polytetrafluoroethylene gaskets were used to set the compressed electrode thickness to within ±2% of the target value. Electrode properties, including compression percentage, measured thickness, and porosity, are shown in **Table 1**.

The flow cell configurations used for pressure drop, EDLC, polarization, and electrochemical impedance spectroscopy (EIS) measurements are shown in **Figure 1**. Interdigitated flow fields (IDFF) were selected for each configuration, as they are commonly used with thin carbon electrodes in flow cells that have demonstrated high power density.[17] Flow-field dimensions are specified in a recent open-source publication.[20] All electrolytes were prepared and stored in an argon-atmosphere glove box (both moisture and oxygen content <1 ppm, Inertcorp, Amesbury, MA) when not in use. Electrolytes at 50% state of charge (SOC) containing 0.05 M total active species concentration were prepared by dissolving 0.025 M (25 mM) of the reduced species (2,2,6,6-tetramethylpiperidin-1-yl)oxyl (TEMPO$^{\bullet}$) (TEMPO radical, 98%, Sigma Aldrich) and 0.025 M (25 mM) of the oxidized species (2,2,6,6-tetramethylpiperidin-1-yl)oxidanyl (TEMPO^{+}) along with 1 M tetraethylammonium tetrafluoroborate ($TEABF_4$, Gotion, 99.45%) into acetonitrile (MeCN, BASF, 99.99%). TEMPO$^{\bullet}$ was chemically oxidized to TEMPO–BF_4 (TEMPO^{+}) using nitrosonium tetrafluoroborate (98%, Alfa Aesar) as described in previous work.[21,22] Neat MeCN was used for pressure drop measurements; 0.25 M potassium hexafluorophosphate (KPF_6, Sigma Aldrich, 99%) in MeCN was used for EDLC measurements; and the polarization measurements used 25 mM TEMPO$^{\bullet}$ and 25 mM TEMPO–BF_4 with 1 M $TEABF_4$ in MeCN. The electrolyte density was determined by aliquoting 1 mL of solution into a tared 20 mL scintillation vial (VWR) three times, obtaining a value of $854.2 \pm 2.5\ \mathrm{kg\,m^{-3}}$.

Table 1. The average ($n = 4$) thickness and vendor specification sheet (#) or calculated (*) porosity measurements for the Freudenberg H23 and AvCarb 1071 electrodes.

Freudenberg H23			AvCarb 1071		
Compression [%]	Thickness [10^{-1} mm]	Porosity [–]	Compression [%]	Thickness [10^{-1} mm]	Porosity [–]
0	2.16 ± 0.02	0.80#	0	3.27 ± 0.05	0.79#
8	1.99 ± 0.04	0.78*	9	2.98 ± 0.01	0.77*
12	1.92 ± 0.01	0.77*	20	2.64 ± 0.00	0.74*
17	1.91 ± 0.01	0.76*	25	2.44 ± 0.01	0.72*
22	1.65 ± 0.01	0.74*	32	2.19 ± 0.01	0.68*

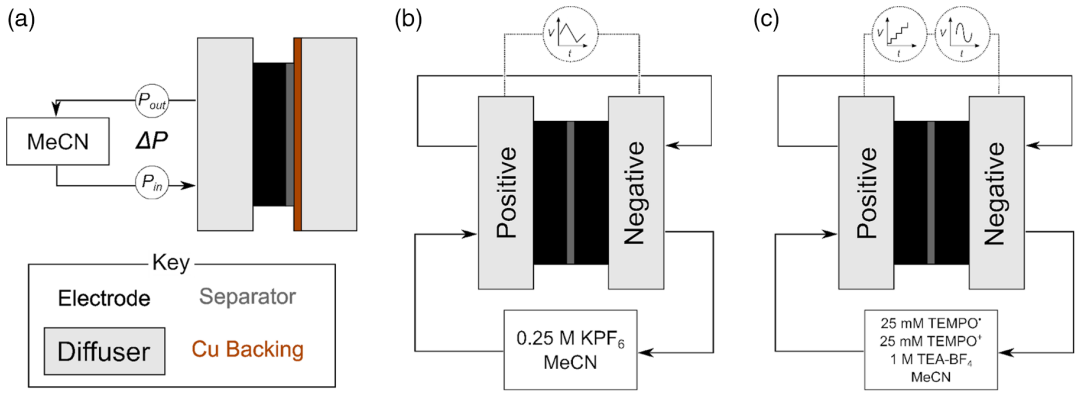

Figure 1. The configurations used for conducting the a) pressure drop, b) electrochemical double-layer capacitance (EDLC), and c) polarization and electrochemical impedance spectroscopy (EIS) measurements.

The electrolyte viscosity was calculated using a vibrational viscometer (V-700 Viscolite, Hydramotion) submerged in ≈15 mL of electrolyte contained in a 20 mL glass scintillation vial; three total measurements were recorded. The measured viscosity was 5.85 ± 0.01 Pa s. Finally, the conductivity was measured by submerging a conductivity probe (914 pH/Conductometer, Metrohm) into ≈15 mL of electrolyte housed in a 20 mL glass scintillation vial. This was repeated for three total measurements and all measurements were performed on the benchtop in ambient atmosphere. Prior to the measurements, the conductivity probe was calibrated to a 111.9 mS cm^{-1} NaCl standard (Metrohm) and rinsed with deionized water. The conductivity of the electrolyte was determined to be 5.61 ± 0.01 mS m^{-1}.

2.2. X-Ray Micro-Computed Tomography (microCT) Measurements

The microCT was conducted by punching 6 mm diameter circular samples of both the AvCarb 1071 and the Freudenberg H23 electrodes. The microCTs used a GE Nanotom scanner (GE Inspection Technologies) with 1.8 µm voxel edge length using a 60 kV tube voltage and 240 µA current with a 500 ms exposure averaged over 5 frames per projection angle, for a total of 1900 projection angles. The compression was manually set in a housing made of polyether ether ketone (PEEK) with a fine pitch thread, which is detailed in Chen et al.[23] The total time for each scan was 1.6 h. The subsequent image segmentation was similar to that in Greco et al.[24] to generate binarized images for quantitative analysis. A schematic of the setup can be found in Figure S1 in Section 1, Supporting Information.

2.3. Ex Situ Compression Measurements

The ex situ compression measurements were carried out on a Zwick Z101 universal testing machine equipped with an Xforce HP load cell (Zwick, 1 kN nominal, 768 210), using a displacement rate of 0.15 mm min^{-1} at a temperature of 23 °C with a max load of 750 N and a resolution of 0.01 N. Sample cutouts of 10 mm diameter were prepared for both electrodes as single specimens and in stacks of five, as well as 24 mm diameter for Freudenberg H23 and 27 mm for AvCarb 1071. The 10 and 24 mm samples were repeated five times, and the 27 mm sample was repeated four times. The diversity of sample sizes was selected to assess the validity of the measurements across different geometries, ensuring high-fidelity results for both electrodes. To ensure good contact between the compression plates and the sample, a pre-load application of 0.5 N was used. A compression test without electrodes was conducted to compensate for machine compliance during the actual tests. A photo of the load cell used in this study is shown in Figure S4 in Section 2, Supporting Information.

2.4. Fluid Dynamic Measurements

The pressure drop across the electrode was measured using the apparatus shown in Figure 1a with MeCN as a proxy for the electrolytes used in subsequent electrochemical measurements,[22,25] consisting of the electrode and a Daramic 175 separator abutted between the IDFF and a Cu-impermeable backing plate. Two digital pressure gauges (100 psi XP2I-DL, MA Selmon, Inc.) were affixed to the inlet and the outlet of the cell, connected with Masterflex L/S 16 tubing. The pressure gauges were set to capture the average pressure at the inlet and the outlet of the cell every second across all electrolyte velocities during 1 min holds. Prior to data acquisition, MeCN was circulated through the assembly at a superficial velocity of 5 cm s^{-1} for 15 min to promote electrode wetting. After the measurement, the electrode was removed from the flow cell and an identical pressure drop measurement was performed to account for hydraulic losses due to the flow field, tubing, and the fittings. All measurements were repeated once.

2.5. Surface Area Measurements

Electrode capacitance was used as an approximate measure of ECSA and was determined by performing cyclic voltammetry (CV) on a single-electrolyte flow cell configuration containing one electrode per side and using a blank electrolyte of 0.25 M KPF_6 in MeCN. KPF_6 was chosen because it was shown to coordinate weakly to the electrode surface, which enabled comparison between EDLC values across different materials.[26]

Specifically, in this configuration (Figure 1b), the electrolyte stream first passed through the positive half-cell and then directly looped through the negative half-cell.[27] For all tests, electrolyte was pumped through the assembly at a volumetric flow rate of 14 mL min^{-1} using a peristaltic pump (Masterflex L/S series model) and norprene tubing (Masterflex L/S 14). Because the volumetric flow rate was fixed, the linear velocity varied; however, ECSA is a steady-state measurement and thus independent of flow rate.[22]

The capacitance was calculated from the slope of the linear relationship between capacitive current (A) and scan rate (V s^{-1}). Scan rates used were 5, 10, 20, 50, 100, and 200 mV s^{-1} with a cell voltage window of −0.1 to 0.1 V. To minimize the convolution of ohmic losses during the experiment, iR_Ω corrections were performed using the high-frequency intercept of Nyquist plots derived from EIS measurements.[28] To isolate the electrode capacitance, the capacitance of a flow cell without electrodes was subtracted from the calculated capacitance of cells with a set of electrodes at each compression level. ECSA of both electrodes was subsequently estimated by normalizing the electrode capacitance by the specific capacitance of graphite in 0.25 M KPF_6 (10 μF cm^{-2}).[26] All tests were performed on the benchtop using a VMP3 Bio-Logic potentiostat (Bio-Logic USA, Knoxville, TN) and repeated once.

2.6. Flow Cell Measurements

Electrode polarization and impedance were measured on the benchtop in a single-electrolyte flow cell with electrolyte at 50% SOC (0.025 M TEMPO / 0.025 M TEMPO-BF_4 / 1 M $TEABF_4$ / MeCN) (Figure 1c) with one electrode used per side betwixt a Daramic 175 separator and superficial electrode velocities of 1, 2.5, and 5 cm s^{-1}. The flow cell was equilibrated under flow at open-circuit voltage (OCV) for 15 min prior to testing. EIS was performed at OCV to identify the kinetic, ohmic, and mass transport contributions to the total DC resistance of the flow cell. Frequencies from 1 to 10 MHz were applied at 6 points per decade with an average of 5 measures per frequency recorded, using a sinus amplitude of 10 mV. Upon completion of EIS, the system was then polarized from 0–0.6 V in 25 mV increments and held at constant potential for 1 min to ensure steady state; the resulting current density was measured, where the last 30 s was averaged and reported. All tests were performed using a VMP3 Bio-Logic potentiostat, and each test was repeated once.

To interpret EIS results, the Nyquist impedance data was fit to a modified Randles circuit to deconvolute the ohmic, kinetic, and mass-transport resistances in the system.[29] EC-Lab software was used to fit the model to the experimental data. To obtain these fits, the initial value of each variable was randomized, and a simplex minimization was performed, where a limit of 5,000 iterations was found to be sufficient for convergence and all χ^2 values were <0.2 (Table S1 and S2, Supporting Information).

2.7. 1D Model Formulation

The single-electrolyte polarization data was fit to a previously studied 1D porous electrode model to extract mass-transfer relationships across each electrode compression.[20] While the details of this model formulation can be found elsewhere,[20] the formation is briefly described in a similar manner to Barton et al.[30] This model related the electrolyte overpotential throughout the electrode position as a second order differential equation

$$\frac{d^2\tilde{\eta}}{d\tilde{x}^2} = \frac{\nu^2\, 2\,\tilde{c}\, \sinh(\frac{\tilde{\eta}}{2})}{1 + 2\,\theta\,\tilde{c}\, \cosh(\frac{\tilde{\eta}}{2})} \tag{1}$$

where $\tilde{\eta}$ is the dimensionless overpotential ($\eta\ F/(R\ T)$, −, $R = 8.3145$ J mol^{-1} K^{-1}, $T = 298$ K, $F = 96\,485$ C mol^{-1}), $\tilde{c}$ is the dimensionless active species concentration ($\tilde{c} = c/c_\theta$, $c_\theta = 1$ M), and $\tilde{x}$ is the dimensionless electrode thickness ($\tilde{x} = x/h$). Both ν^2 and θ are fitting parameters that, in their definitions, include properties related to the electrode and system. θ represents the ratio of the exchange current density (i_0, A m^{-2}) to the limiting current density (i_l, A m^{-2}), defined as follows

$$\theta = \frac{i_0}{i_l} \tag{2}$$

where i_0 can be formulated through Equation (3)

$$i_0 = n\,F\,k_a\,c_\theta\, \exp\left(\frac{\alpha\, n\, F\, V_\theta}{R\,T}\right) \tag{3}$$

with k_a (m^2 s^{-1}) as the anodic rate constant. V_θ (V) can be described as the change in potential across the electrode and electrolyte interfaces, which is related to the cathodic rate constants k_c (m s^{-1}) through Equation (4).

$$V_\theta = \frac{R\,T}{n\,F}\log\left(\frac{k_c}{k_a}\right) \tag{4}$$

i_l can be approximated as follows

$$i_l = n\,F\,k_m\,c_\theta \tag{5}$$

where k_m (m s^{-1}) is the mass-transfer coefficient. Effectively, Equation (5) represents the local limiting current in the electrode that assumed the surface concentration was negligible and equivalent to the flux of current generated from active species transport to the surface.

Similarly, ν^2, which serves as a ratio between the reaction and charge transport rates, is defined as follows

$$\nu^2 = \frac{F\,a\,i_0\,h^2}{k_{eff}\,R\,T} \tag{6}$$

where a is the volumetric surface area (m^2 m^{-3}) and k_{eff} is the effective electrolyte conductivity, which was estimated through the Bruggeman correction by the electrolyte conductivity (k, S m^{-1}) as $k_{eff} = k\,\varepsilon^{1.5}$.

With the separator at position $x = 0$ and the flow field at $x = h$, the boundary conditions could be formulated, assuming the overpotential at $x = 0$ is half of the iR-corrected cell potential (ϕ_s, V), described as follows

$$\tilde{\eta}|_{x=0} = \frac{\phi_s F}{2 R T} \tag{7}$$

Additionally, the current density was assumed to be zero at the $x = h$ interface, relating the ionic current density (j, A m^{-2}) to the overpotential. The boundary condition is defined as follows

$$j|_{x=h} = \frac{1}{2}\frac{d\eta}{dx}\bigg|_{x=h} = 0 \tag{8}$$

or, in dimensionless form,

$$\tilde{j}|_{\tilde{x}=1} = \frac{1}{2}\frac{d\tilde{\eta}}{d\tilde{x}}\bigg|_{\tilde{x}=1} = 0 \tag{9}$$

where $\tilde{j}$ can be related to j through Equation (10)

$$\tilde{j} = \frac{j F h}{2 k_{\text{eff}} R T} \tag{10}$$

With the fitted parameters θ (−) and ν^2 (−), the volumetric surface area mass-transfer coefficient ($a{\cdot}k_m$, s^{-1}) can be extracted through the following relationship

$$a{\cdot}k_m = \frac{\nu^2}{\theta}\frac{k_{\text{eff}} R T}{F^2 h^2 c} \tag{11}$$

With estimations for a from the EDLC experiments, the critical mass-transfer length scale (l_c, m), and the diffusivity (D, m^2 s^{-1}), the dimensionless Sherwood (Sh) and Péclet (Pe) numbers can be defined as follows

$$Pe = \frac{\nu l_c}{D} \tag{12}$$

$$Sh = \frac{a{\cdot}k_m l_c}{a D} = \frac{\nu^2 k_{\text{eff}} R T l_c}{\theta F^2 h^2 a D} \tag{13}$$

These simulations were solved in MATLAB R2020a using a 6-core laptop with 64 GB RAM with Intel Core i7-9750H CPUs (2.60 GHz) requiring ≈60 s to compute a fit for each compression.

3. Results and Discussion

3.1. MicroCT Analysis

The microCT images of the Freudenberg H23 and AvCarb 1071 electrodes were binarized in a similar method as previously reported[24] and analyzed using PoreSpy,[31] an open-source software, following a 1250 square pixel crop using Fiji/ImageJ to reduce the file size. Within PoreSpy, the tensorial porosities were extracted across each electrode and its corresponding compression, as shown in **Figure 2**, where x and y are the in-plane directions, and the z is the through-plane direction. Noticeably, the Freudenberg H23 demonstrates similar porosity values throughout each scanning direction, with more stochasticity in the x and y directions. Conversely, the x and y porosity profiles for the AvCarb 1071 have a smoother profile, afforded by the woven bundles that engender an anisotropic—or ordered—electrode rendering. The z directions for the Freudenberg H23 and the AvCarb 1071 show upward tailing, due to the added void space that could not be segmented out of the image—this is more noticeable in the AvCarb 1071, as the fibrous bundles

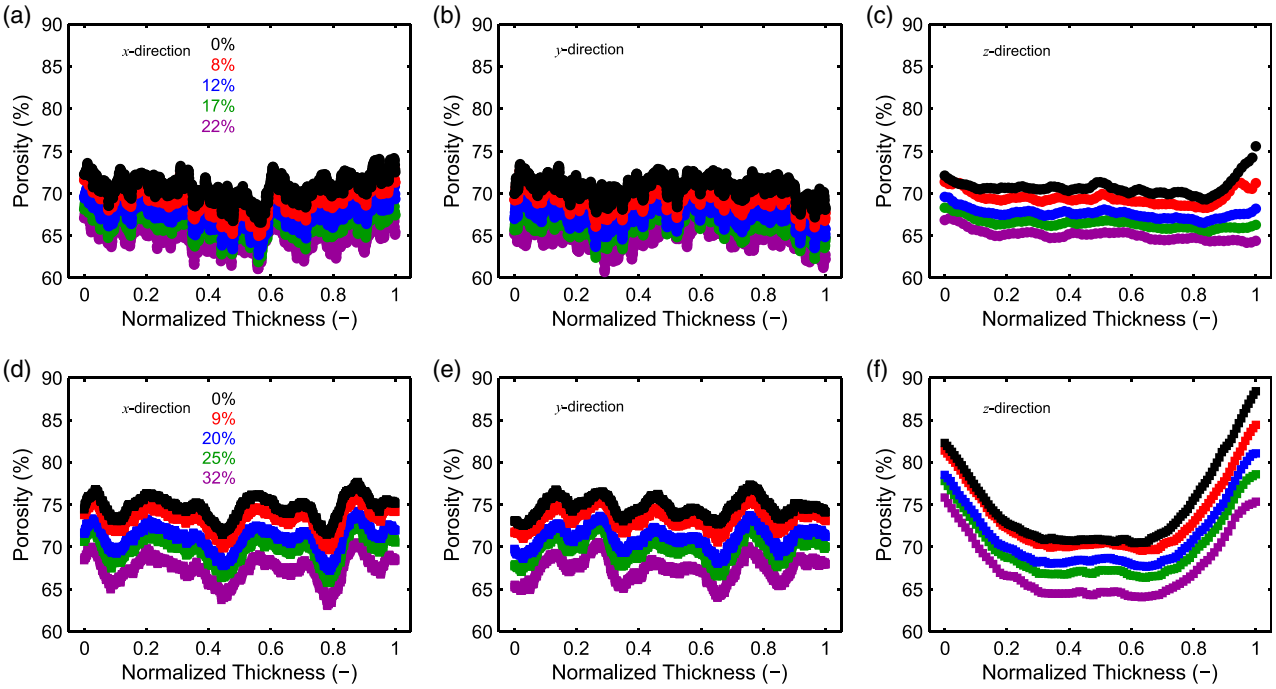

Figure 2. a–c) The x, y, and z porosity profiles for Freudenberg H23 and d–f) AvCarb 1071 with select micro-computed tomography (microCT) images shown in Section 1, Supporting Information.

engender an oscillatory-like domain on the surface of the through-plane view.

3.2. Ex Situ Compression

The ex situ compression enables a direct comparison between the two materials' mechanical robustness under different loads. The load-displacement curves were corrected by removing the displacement contribution relevant to the machine compliance, enabling a proper measurement of the mechanical properties of the materials. The electrode thickness was taken at the start of the measurement by using the distance between the plates to establish a baseline for the compressive procedure. The material stress was evaluated by dividing the force applied by cross-sectional area, and the strain was set as the change in the electrode thickness divided by the initial uncompressed value. A focus on the initial part of the average stress–strain curves for the 10 mm specimen size is shown in **Figure 3**, with the complete set of stress–strain curves shown in Figure S5, Supporting Information. Different electrode diameters, as well as the single and stacked configurations were tested to validate the experimental procedure. The good agreement between the intensive material properties in different configurations for each material confirms the reliability of the results.

The stress–strain curves of both materials, shown in Figure 3, display two regions with different trends. At first, the stress increases almost linearly with the strain and the response is similar between the two materials. At a certain level of strain, larger in the case of AvCarb 1071 with respect to Freudenberg H23, the stress starts to increase more rapidly in a nonlinear fashion. This behavior can be explained with the porosity of these materials: in the first region, the materials are compacted, and the air pockets are squeezed out and decrease the fiber-to-fiber spacing. The electrode then progressively displays a continuum of increasing stiffness.

In comparing the stress–strain responses between the two electrodes, the AvCarb 1071 electrode shows a larger initial region and generally demonstrates greater compliance to compression, as compared to the Freudenberg H23 electrode. Further, these results suggest that the AvCarb 1071 electrode may be able to withstand higher levels of compression than previously studied; for example, previous work using the same chemistries has operated between 20–30%,[22,25] which is still below common carbon felt compressions (40–50%).[11–13] Higher electrode compression is typically desirable due to the reduction in contact resistance, but over-compression could lead to limited improvements in electrochemical performance by hindering mass transport that could, in turn, lead to leaking.[32]

3.3. Pressure Drop

Pressure drop reveals the changes of fluid-dynamic relationships with neat MeCN, a known wetting solvent,[22,25] as the electrodes undergo compression. For all electrode compression and fluid velocities, Darcy's law can be used for extracting a combined through-plane and in-plane permeability value (κ, m^2). This was done for each electrode and compression degree using Equation (14).

$$\frac{\Delta P}{L} = \frac{\mu}{\kappa} v \tag{14}$$

where L is the advective length scale (1 mm), μ is the viscosity of MeCN (3.43 mPa s[33]) and v is the superficial velocity (m s^{-1}).

The Freudenberg H23 electrode shows plateaued κ values from 0–8% compression (**Figure 4**), suggesting an improvement in hydraulic pathways that, at high compressions, become obfuscated, as evinced by the lower κ values at higher compressions. In general, the carbon cloths report higher κ values compared to carbon papers, which is in agreement with previous studies.[25] However, across the ranges investigated, the carbon cloths appear less sensitive to increased compression, as evinced by the small changes in κ and moderate stress–strain relationships (Figure 3). This is likely due to the bimodal pore structure of the cloth, with large pores that allow electrolyte to flow through the material unobstructed.[25] The difference in values both within and between electrode materials implies variable material mechanics directly influence the effective fluid-dynamic pathways within the flow cell. Importantly, the solvent, MeCN, used in this study is a better wetting solvent than water, indicating these findings may vary based upon electrolyte composition under different forced advective pathways (a la flow field).

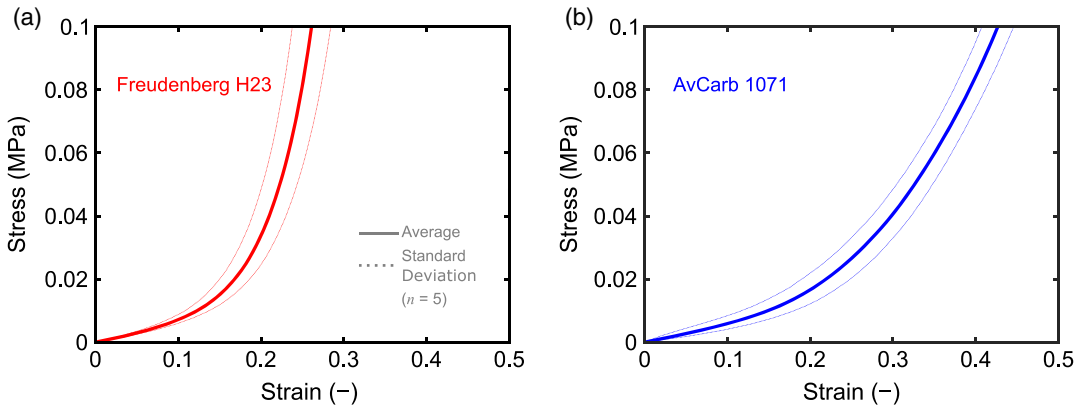

Figure 3. The average and standard deviation ($n = 5$) stress–strain curves for a) Freudenberg H23 and b) AvCarb 1071 electrodes using 10 mm diameter samples.

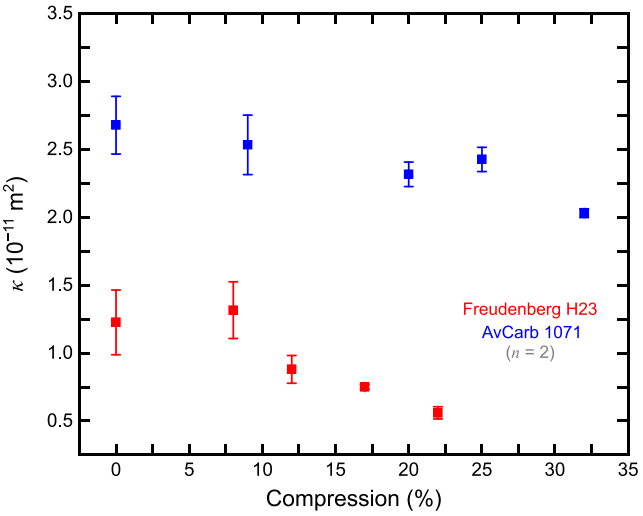

Figure 4. The average ($n = 2$) κ values across the compression values for Freudenberg H23 and AvCarb 1071.

The raw data used in generating Figure 4 can be found in Section 4 of the Supporting Information.

3.4. EDLC

EDLC measurements were performed to estimate the surface area of electrodes and observe how the accessible surface area is affected by compression. We find that the ECSA values are nearly identical across the range of electrode compressions, indicating that moderate compressions do not restrict available surface area (**Table 2**). There is considerable sample-to-sample variability in the measured ECSA of Freudenberg H23 electrodes, likely due to varying thickness of the material throughout the bulk—we found that measured values for electrode thickness varied up to 12.5% (≈0.21–0.24 mm) depending on the area that the electrode was cut from the 25 × 25 cm^2 piece provided by the vendor—however, there is no general trend observed with increasing compression. For AvCarb 1071, there is generally a step change from lower compression (0–10%) to higher compression (20–32%) indicating that the large pores in the cloth enable high electrode accessibility even at high compressions. Additionally, we find that the cloth has lower total ECSA than Freudenberg, although the sample-to-sample variation is reduced. While EDLC measurements under different compressions for Freudenberg H23 and AvCarb 1071 have not been widely studied, we can compare our findings with those reported in literature. Forner-Cuenca et al. found ECSA values of 0.15 ± 0.01 and $0.050 \pm 0.004\ m^2\ g^{-1}$ for the Freudenberg H23 at ≈23% compression and for the AvCarb 1071 at ≈15% compression, respectively,[25] which is in good agreement with the range of ECSA values presented in this study. Similarly, Tenny et al. employed higher compressions for the AvCarb 1071 (30%) and reported an average ECSA value of $0.048 \pm 0.000\ m^2\ g^{-1}$, also agreeing with the results in this study.[22] Notably, both Forner-Cuenca et al. and Tenny et al. used different experimental setups in their work; specifically, both used a flow through flow field with 0.1 M $TEABF_4$[25] and 1.0 M $TEABF_4$,[22] which may influence the values, but the magnitudes are similar, which we hypothesize is due to the identical solvent (i.e., neat MeCN) used in all studies.

Table 2. Estimated electrochemically active surface area (ECSA) from electrochemical double-layer capacitance (EDLC) measurements for both Freudenberg H23 and AvCarb 1071 ($n = 2$).

Freudenberg H23		AvCarb 1071	
Compression [%]	ECSA [$m^2\ g^{-1}$]	Compression [%]	ECSA [$m^2\ g^{-1}$]
0	0.14 ± 0.03	0	0.083 ± 0.009
8	0.098 ± 0.024	9	0.093 ± 0.007
12	0.096 ± 0.035	20	0.053 ± 0.000
17	0.13 ± 0.00	25	0.051 ± 0.008
22	0.11 ± 0.02	32	0.071 ± 0.003

3.5. Polarization and EIS

EIS and polarization measurements were performed in a single-electrolyte flow cell to understand the effect of compression on electrode performance. EIS measurements taken at OCV were fitted to a modified Randles circuit, similar to previous work.[25,29] We obtained reasonable fits, with chi-square values of ≤0.2 (Section 3 of Supporting Information). The values from these fits are used to deconvolute the resistance contributions of the ohmics, kinetics, and mass transport, providing a semi-qualitative relationship to the different electrode compressions (**Figure 5**). Notably, the AvCarb 1071 exhibits higher ohmic resistance compared to the Freudenberg H23, a phenomenon seen in prior reports[25]; we postulate that this is due to differences in contact resistance at the electrode–flow field interface, due to the curvature of the weave, which may lead to reduced points of contact. Nevertheless, the magnitude of the kinetic and mass-transfer resistances is similar. To evaluate electrode performance as a function of compression, we measured polarization in a single-electrolyte flow cell with both AvCarb 1071 and Freudenberg H23 at each compression (**Figure 6**). The presented polarization results are iR-corrected to deconvolute the impact of ohmic contributions from mass-transfer and kinetic behavior. We find that the ohmic resistance does not decrease as a function of compression; rather, an initial decrease in ohmic resistance is observed up to moderate compressions for both materials (12% and 20% for Freudenberg H23 and AvCarb 1071, respectively), before increasing upon further compression (Figure 5a). We expected that ohmic resistance would decrease as contact resistance decreases[13]; however, it is possible that contact resistance increases as the electrode is compressed to the point that it intrudes into the flow channels of the IDFF, resulting in uneven contact with the flow field and/or membrane, indicating the importance of in situ measurements, particularly with different electrode and flow-field combinations.[34] We measured polarization at a range of superficial electrolyte velocities (1, 2.5, and 5 $cm\ s^{-1}$) and saw that across electrode compressions, as flow rate increases, the overpotential decreases. We find that the Freudenberg H23 electrode performance varies

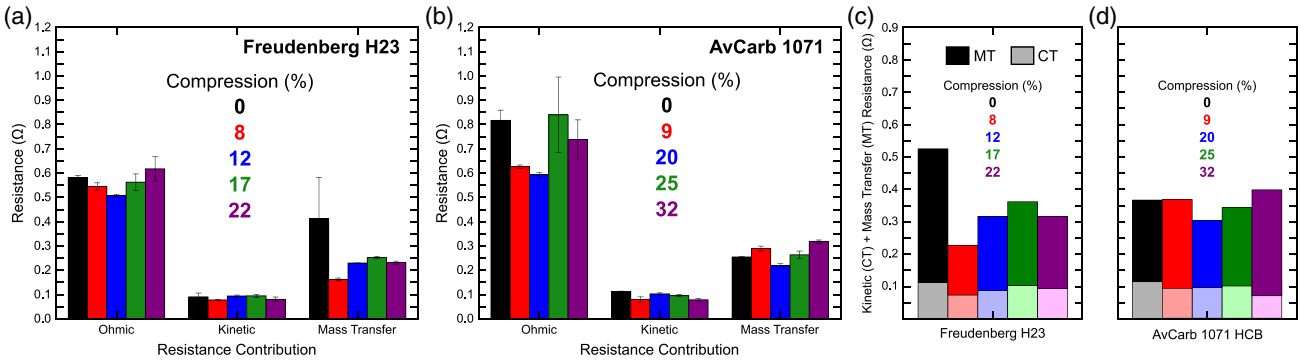

Figure 5. The ohmic, kinetic, and mass-transfer resistance contributions to the modified Randles circuit ($n = 2$) for a) FH23 and b) 1071HCB at 5 cm s^{-1}. The combined kinetic (CT) and mass-transfer (MT) resistance for the c) Freudenberg H23 and d) AvCarb 1071.

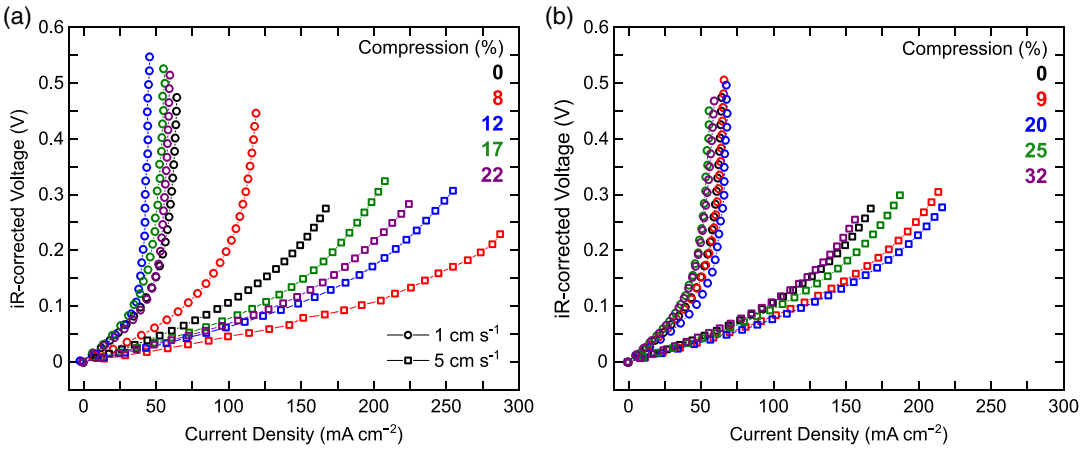

Figure 6. iR-corrected overpotential of single-electrolyte flow cells with a) Freudenberg H23 and b) AvCarb 1071 electrodes at different compressions.

significantly at different compressions and the best performance is observed at 8% compression. We postulate that this improvement over uncompressed electrodes are due to a reduction in mass-transfer resistance (Figure 5a), due to enhanced contact between electrode and flow field that may lead to increased availability of electrolyte flow paths. However, compression beyond 8% leads to mass transport limitations due to decreasing pore size and subsequent reduction in permeability, leading to increased overpotential. Importantly, AvCarb 1071 performance is less variable, and all compressions perform relatively similarly, suggesting the cloth structure is more robust to the physical deformations and deliver similar electrochemical outputs, which can be useful for stack assemblies.[35] The best AvCarb 1071 performance occurs at 20% compression and decreases at greater compressions, likely due to a similar, but less stark, phenomenon observed for Freudenberg H23 electrodes. It is likely that, due to the large pores present within the cloth, the material is more tolerant to greater compression, as these large pores continue to provide unrestricted flow of electrolyte even at higher compression.[25] When compared to EIS (Figure 5c), the polarization trends appear to align with the combined kinetic and mass-transfer resistances. Similarly, the best polarization performances, which occur at 8% and 20% compression for Freudenberg H23 and AvCarb 1071, respectively, align with the lowest combined kinetic and mass-transfer resistances.

3.6. Transport Scaling

The resulting $a{\cdot}k_m$ values from the 1D model polarization fitting plotted against ΔP are shown in **Figure 7**a,b, demonstrating the comparative mass-transport and fluid-dynamic scaling. Notably, the top performers from the 5 cm s^{-1} polarization also correspond with the highest $a{\cdot}k_m$ quantities—specifically, the 8% Freudenberg H23 and 20% AvCarb 1071 electrodes. Interestingly, across the different superficial velocities tested, the scaling between the $a{\cdot}k_m$ and $\Delta P\ L^{-1}$ does not explicitly follow the polarization trends. We hypothesize this may be due to the variations in the advective and mass-transport boundary layer formation across the compressions stemming from complicated intraelectrode velocity fields influenced by the IDFF. For example, similar mass-transfer and fluid-dynamic scaling by Tenny et al. using the AvCarb 1071 electrode in a flow-through flow field, showed an exponential relationship of 0.97,[22] which is outside the relatively insensitive range of 0.56–0.57 for 25–32% compression in this study, suggesting that, despite materials insensitivity toward compression, the AvCarb 1071 possesses flow-field sensitivities. Indeed, the flow-field topology has been shown to elicit variations in transport scaling across similar electrodes in other electrochemical environments,[20,36,37] underscoring the importance of properly matching electrode structures to complementary fluidic environments.

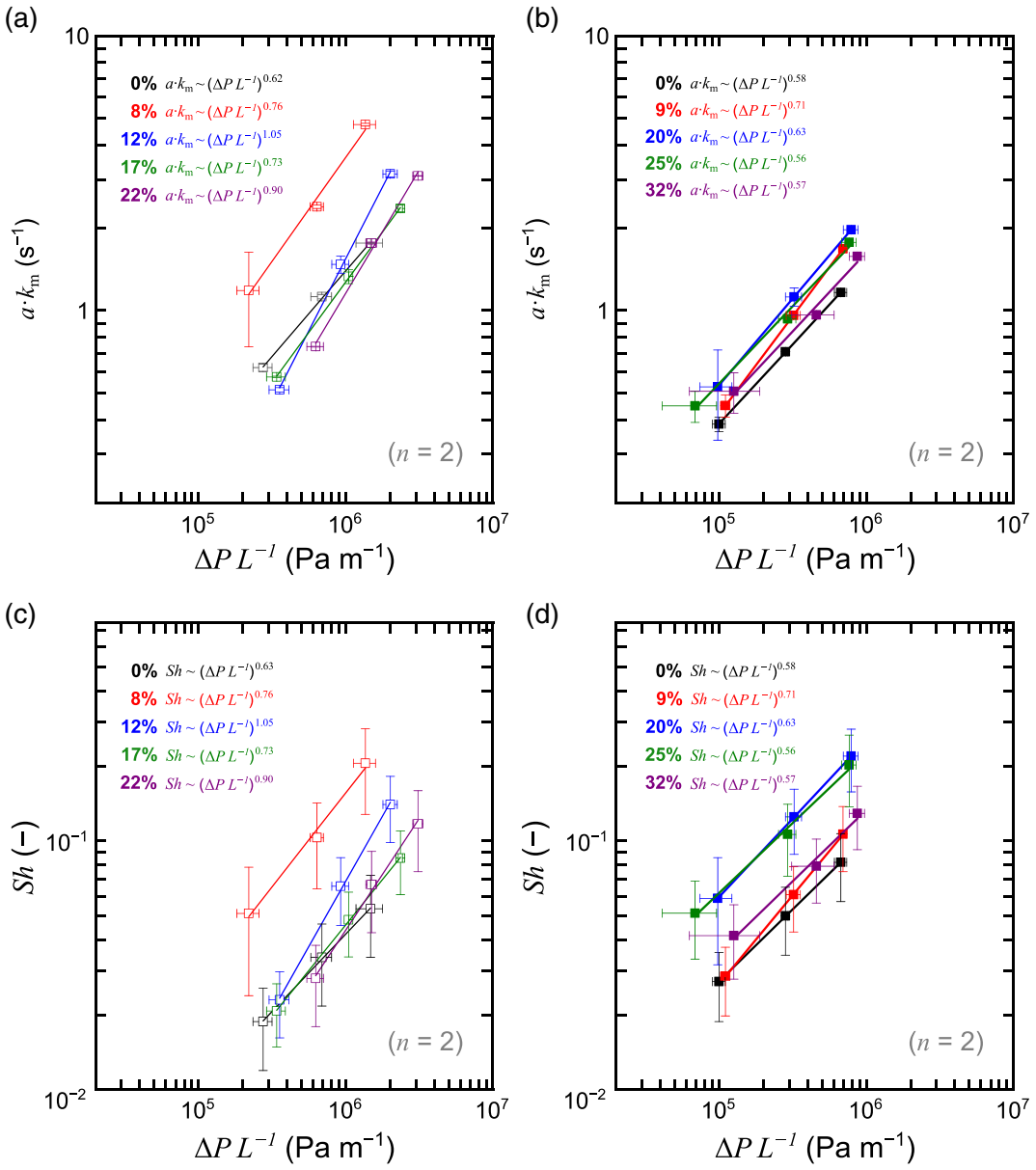

Figure 7. The $a{\cdot}k_m$ plotted against the $\Delta P\ L^{-1}$ for the a) Freudenberg H23 and b) AvCarb 1071 electrodes, along with their exponential scaling. Additionally, the *Sh* plotted against $\Delta P\ L^{-1}$ for the c) Freudenberg H23 and d) AvCarb 1071 electrodes, along with their exponential scaling.

Using the results from the 1D model and the EDLC measurement, the *Sh* can be obtained using Equation (13), with l_c defined as the fiber diameter (Freudenberg H23 is 10 µm[25] and AvCarb 1071 is 7.5 µm[22]) and D as the average TEMPO$^{(\bullet/+)}$ diffusivity value reported in Tenny et al.[22] Generally, the Freudenberg H23 electrode across different compressions have higher *Sh* values than those of the AvCarb 1071, aligning with the polarization and resistance values. Additionally, the AvCarb 1071 electrodes reveal less spreading of *Sh* values across the different $\Delta P\ L^{-1}$ values, agreeing with the fluid dynamic and the ex situ compressive load tests of possessing more mechanical robustness than the Freudenberg H23 electrodes (vide supra).

4. Conclusions

Overall flow battery operation can be influenced by electrode morphology and compression for a particular advective environment. To date, there have been few studies exploring the impact of compressive load on the structural features of different carbon electrodes as well as their fluid-dynamic and electrochemical performance. Leveraging microCT imaging, load cell testing, and fluid-dynamic and electrochemical metrics, we compare the changes to pressure loss, polarization, and mass-transfer scaling with a carbon paper (Freudenberg H23) and cloth (AvCarb 1071) electrode under five different compressions, which span the

range typically reported in the open literature. Testing within a $TEMPO^{(\bullet/+)}$ redox couple dissolved in a low-viscosity, wetting electrolyte, we observed a direct relationship between electrochemical performance and bulk permeability measurements of the Freudenberg H23. However, the AvCarb 1071 electrode demonstrated a higher compliance under a compressive load, as compared to the Freudenberg H23, resulting in a relative insensitivity between changes in the tested compression range and computed permeability values.

Assessing the various resistance contributions through fitting Nyquist impedance plots to a modified Randles circuit, we found the Freudenberg H23 exhibited lower combined ohmic, charge-transfer, and mass-transport values, resulting in improved electrochemical performance across all compressive values, as compared to the AvCarb 1071 electrode. These electrochemical performance metrics continue in dimensionless *Sh* analysis when compared to the $\Delta P\ L^{-1}$, demonstrating lower values, despite the lower pressure drop. However, when compared with similar, nonaqueous studies, the mass-transport and fluid-dynamic scaling of the AvCarb 1071 is lower in this work, which we hypothesize is due to variations in flow-field determining advective pathways throughout the electrode during operation.

Additionally, this study shows that moderate compressions of Freudenberg H23 (8%) in a kinetically fast, electrode-wetting environment led to improvements in overall RFB operation, but we posit that optimal electrode compressions are electrolyte and flow-field specific, necessitating further studies under a wider range of compressions to draw broader relationships across chemical environments. Overall, the Freudenberg H23 exhibits a greater sensitivity to compression with peak electrochemical activity correlating with increased permeability, and the AvCarb 1071 remains relatively insensitive to compressive loads with lower, yet less variable, electrochemical performance. These findings demonstrate the trade-offs of mechanical robustness on fluid-dynamic and electrochemical performance between the Freudenberg H23 and the AvCarb 1071, suggesting each could be used for specific operating environments. For example, RFB stacks, comprising multiple flow cells sandwiched together, could benefit from a mechanically robust electrode with similar electrochemical performance, as shown in the carbon cloth. While this study was conducted under predefined electrochemical conditions, further cell-level diagnostics, that incorporate electrode structures, electrolyte selections, flow-field geometries, are needed for holistic operational analysis in identifying target electrode selection for specific RFB usage and extensions into stack-level applications.

Supporting Information

Supporting Information is available from the Wiley Online Library or from the author.

Acknowledgements

K.M.T. and K.V.G. contributed equally to this work. This work was supported by the Joint Center for Energy Storage Research, an Energy Innovation Hub funded by the US Department of Energy Office of Science, Basic Energy Sciences. K.M.T. and K.V.G. acknowledge additional financial support from the NSF Graduate Research Fellowship (Grant no. 1122374). Any opinion, findings, and conclusions or recommendations expressed in this material are those of the authors and do not necessarily reflect the views of the National Science Foundation. M.V.D.H. and A.F.-C. acknowledge funding from the Dutch Research Council (NWO) for the Veni Grant (Grant no. 17324). A.M. acknowledges funding form the Swiss National Science Foundation (Grant no. 169913). We would like to thank Professor Leon E. Govaert for insightful comments and feedback throughout this work.

Conflict of Interest

The authors declare no conflict of interest.

Author Contributions

K.M.T.: Conceptualization, Methodology, Validation, Formal analysis, Investigation, Data curation, Writing—original draft, Writing—review & editing, Visualization, Project administration. K.V.G.: Conceptualization, Methodology, Validation, Formal analysis, Investigation, Data curation, Writing—original draft, Writing—review & editing, Visualization, Project administration. M.V.D.H.: Conceptualization, Methodology, Writing—review & editing. T.P.: Formal analysis, Writing—review & editing. A.M.: Validation, Investigation, Data curation, Writing—review & editing. J.E.: Validation, Investigation, Data curation, Writing—review & editing. A.F.-C.: Conceptualization, Writing—review & editing, Supervision, Funding acquisition. Y.-M.C.: Resources, Funding acquisition. F.R.B.: Resources, Writing—original draft, Writing—review & editing, Funding acquisition.

Data Availability Statement

The data that support the findings of this study are available from the corresponding author upon reasonable request.

Keywords

compression, microCT, mass transfer, porous electrodes, redox flow batteries

Received: December 29, 2021
Revised: March 8, 2022
Published online: June 14, 2022

[1] Z. Yang, J. Zhang, M. C. W. Kintner-Meyer, X. Lu, D. Choi, J. P. Lemmon, J. Liu, *Chem. Rev.* **2011**, *111*, 3577.
[2] M. Skyllas-Kazacos, M. H. Chakrabarti, S. A. Hajimolana, F. S. Mjalli, M. Saleem, *J. Electrochem. Soc.* **2011**, *158*, R55.
[3] W. Wang, Q. Luo, B. Li, X. Wei, L. Li, Z. Yang, *Adv. Funct. Mater.* **2013**, *23*, 970.
[4] Z. Yang, J. Liu, S. Baskaran, C. H. Imhoff, J. D. Holladay, *JOM* **2010**, *62*, 14.
[5] G. Kear, A. A. Shah, F. C. Walsh, *Int. J. Energy Res.* **2012**, *36*, 1105.
[6] R. M. Darling, K. G. Gallagher, J. A. Kowalski, S. Ha, F. R. Brushett, *Energy Environ. Sci.* **2014**, *7*, 3459.
[7] M. L. Perry, A. Z. Weber, *J. Electrochem. Soc.* **2016**, *163*, A5064.
[8] M. H. Chakrabarti, N. P. Brandon, S. A. Hajimolana, F. Tariq, V. Yufit, M. A. Hashim, M. A. Hussain, C. T. J. Low, P. V. Aravind, *J. Power Sources* **2014**, *253*, 150.
[9] T.-C. Chang, J.-P. Zhang, Y.-K. Fuh, *J. Power Sources* **2014**, *245*, 66.
[10] P. C. Ghimire, A. Bhattarai, R. Schweiss, G. G. Scherer, N. Wai, Q. Yan, *Appl. Energy* **2018**, *230*, 974.

[11] J. Charvát, P. Mazúr, J. Dundálek, J. Pocedič, J. Vrána, J. Mrlík, J. Kosek, S. Dinter, *J. Energy Storage* **2020**, *30*, 101468.
[12] R. Gundlapalli, S. Jayanti, *J. Power Sources* **2019**, *427*, 231.
[13] S.-K. Park, J. Shim, J. H. Yang, C.-S. Jin, B. S. Lee, Y.-S. Lee, K.-H. Shin, J.-D. Jeon, *Electrochim. Acta* **2014**, *116*, 447.
[14] K. Oh, S. Won, H. Ju, *Electrochim. Acta* **2015**, *181*, 13.
[15] D. S. Aaron, Q. Liu, Z. Tang, G. M. Grim, A. B. Papandrew, A. Turhan, T. A. Zawodzinski, M. M. Mench, *J. Power Sources* **2012**, *206*, 450.
[16] Q. H. Liu, G. M. Grim, A. B. Papandrew, A. Turhan, T. A. Zawodzinski, M. M. Mench, *J. Electrochem. Soc.* **2012**, *159*, A1246.
[17] R. M. Darling, M. L. Perry, *J. Electrochem. Soc.* **2014**, *161*, A1381.
[18] V. Radhakrishnan, P. Haridoss, *Mater. Des.* **2011**, *32*, 861.
[19] A. M. Pezeshki, J. T. Clement, G. M. Veith, T. A. Zawodzinski, M. M. Mench, *J. Power Sources* **2015**, *294*, 333.
[20] J. D. Milshtein, K. M. Tenny, J. L. Barton, J. Drake, R. M. Darling, F. R. Brushett, *J. Electrochem. Soc.* **2017**, *164*, E3265.
[21] J. D. Milshtein, A. P. Kaur, M. D. Casselman, J. A. Kowalski, S. Modekrutti, P. L. Zhang, N. Harsha Attanayake, C. F. Elliott, S. R. Parkin, C. Risko, F. R. Brushett, S. A. Odom, *Energy Environ. Sci.* **2016**, *9*, 3531.
[22] K. M. Tenny, A. Forner-Cuenca, Y.-M. Chiang, F. R. Brushett, *J. Electrochem. Energy Convers. Storage* **2020**, *17*, 041108.
[23] Y.-C. Chen, A. Berger, S. De Angelis, T. Schuler, M. Bozzetti, J. Eller, V. Tileli, T. J. Schmidt, F. N. Büchi, *ACS Appl. Mater. Interfaces* **2021**, *13*, 16227.
[24] K. V. Greco, A. Forner-Cuenca, A. Mularczyk, J. Eller, F. R. Brushett, *ACS Appl. Mater. Interfaces* **2018**, *10*, 44430.
[25] A. Forner-Cuenca, E. E. Penn, A. M. Oliveira, F. R. Brushett, *J. Electrochem. Soc.* **2019**, *166*, A2230.
[26] Y. Yoon, B. Yan, Y. Surendranath, *J. Am. Chem. Soc.* **2018**, *140*, 2397.
[27] R. M. Darling, M. L. Perry, *ECS Trans.* **2013**, *53*, 31.
[28] A. M. Pezeshki, R. L. Sacci, F. M. Delnick, D. S. Aaron, M. M. Mench, *Electrochim. Acta* **2017**, *229*, 261.
[29] T. Liu, X. Li, C. Xu, H. Zhang, *ACS Appl. Mater. Interfaces* **2017**, *9*, 4626.
[30] J. L. Barton, J. D. Milshtein, J. J. Hinricher, F. R. Brushett, *J. Power Sources* **2018**, *399*, 133.
[31] J. Gostick, Z. A. Khan, T. G. Tranter, M. D. R. Kok, M. Agnaou, M. A. Sadeghi, R. Jervis, *J. Open Source Softw.* **2019**, https://doi.org/10.21105/joss.01296.
[32] J. Xiong, Y. Song, S. Wang, X. Li, J. Liu, C. Yan, A. Tang, *J. Power Sources* **2019**, *431*, 170.
[33] http://www.inchem.org/documents/icsc/icsc/eics0088.htm
[34] S. Kumar, S. Jayanti *J. Power Sources* **2017**, *360*, 548.
[35] X. Ke, J. M. Prahl, J. I. D. Alexander, J. S. Wainright, T. A. Zawodzinski, R. F. Savinell, *Chem. Soc. Rev.* **2018**, *47*, 8721.
[36] C. R. Dennison, E. Agar, B. Akuzum, E. C. Kumbur, *J. Electrochem. Soc.* **2016**, *163*, A5163.
[37] Q. Wu, X. Zhang, Y. Lv, L. Lin, Y. Liu, X. Zhou, *J. Mater. Chem. A* **2018**, *6*, 20347.